JOURNAL OF SPACECRAFT AND ROCKETS
Vol. 45, No. 3, May–June 2008

Evolutionary Algorithm Shape Optimization of a Hypersonic Flight Experiment Nose Cone

N. R. Deepak,* T. Ray,† and R. R. Boyce‡
University of New South Wales,
Australian Defence Force Academy, Canberra, New South Wales 2600, Australia

DOI: 10.2514/1.33826

Hypersonic vehicle development, particularly for hypersonic airbreathers, will require robust-design optimization to achieve performance targets. Vehicle shape optimization will play an important role. This paper presents the first application to hypersonic vehicle shape optimization of a reduced parametric section shape representation coupled with a surrogate-assisted evolutionary-algorithm optimization approach. The particular case considered is the minimization of total drag of the nose cone of a hypersonic flight experiment. The computational fluid dynamics solver used here is ANSYS CFX. Single-point optimization at Mach 3 and Mach 8 is performed at altitudes relevant to those Mach numbers for a typical hypersonic flight experiment ascent trajectory. Without surrogate assistance, the optimized shapes for each Mach number were both found to result in significant drag-force reductions (1.39% at Mach 3 and 1.96% at Mach 8) when compared with the baseline blunted standard ogive nose-cone shape. When the surrogate assistance (which is a radial-basis-function network approximation to the drag dependence on the shape parameters) was introduced, the optimized shapes yielded nearly the same drag reduction as without surrogate assistance, but also resulted in significant savings in the computational cost. Finally, the performance of the optimum shape derived at Mach 3 is evaluated at Mach 8 and vice versa to illustrate the robustness of the nose-cone shapes derived using such an approach.

Nomenclature

a	=	real coefficient
C	=	children population
C_D	=	drag coefficient
I	=	individual population
L	=	length, m
M	=	individual population
M_∞	=	Mach number
P	=	parent population
p	=	pressure, Pa
S	=	individual from M population
$\mathcal{U}$	=	uniform random number
x	=	initialized variable
y	=	offspring
α	=	angle of attack, deg
γ	=	ratio of specific heats, C_p/C_v
τ_x	=	wall shear stress

Subscripts

i	=	variable number
j	=	constraints
k	=	objectives
n	=	coefficient numbers
∞	=	freestream conditions

Presented as Paper 7998 at the 14th AIAA/AHI International Spaceplanes and Hypersonic Systems and Technologies Conference, Canberra, Australia, 6–9 November 2006; received 2 August 2007; revision received 31 October 2007; accepted for publication 1 November 2007.

*Ph.D. Student, School of Aerospace, Civil and Mechanical Engineering. Student Member AIAA.

†Senior Lecturer, School of Aerospace, Civil and Mechanical Engineering. Member AIAA.

‡Currently DSTO Chair for Hypersonics, Division of Mechanical Engineering, University of Queensland. Senior Member AIAA.

I. Introduction

CONSIDERABLE effort is being invested worldwide in the development of hypersonic airbreathers. Several nations throughout North America, Europe, and the Asia–Pacific region are actively pursuing this technology by using complementary ground-test (experimental and numerical) and flight-test programs. Most of the work so far has necessarily focused on studies of fundamental phenomena using simple configurations. Operational scramjet-powered vehicles will, however, walk a fine line between efficient thrust production and very high drag levels, and this will be achieved only by combining the fundamental concepts in potentially complex 3D configurations. Optimal designs may fall within extremely localized ranges of parameter/geometry variations, may thus easily be missed in a manual top-down design process, and may represent too great a risk if forced to operate off-design. Methods for using fundamental knowledge to generate these optimal designs are required. This is achievable by coupling the science of multidisciplinary design optimization (MDO) to appropriately validated computational fluid dynamics (CFD) simulations of the vehicle flowfields. However, the road to such a capability is best trod step by step, beginning with noncombusting axisymmetric laminar flowfields and working toward 3D turbulent combusting scramjet flowpaths. In this way, the coupling of the CFD and MDO approaches can itself be studied and optimized for computationally tractable cases before attempting the more complex cases. This paper presents such a study for the example of the shape optimization of the nose cone for a rocket-launched ballistic-trajectory hypersonic flight experiment. In particular, it presents the first application to hypersonic vehicle shape optimization of a reduced parametric section (PARSEC) approach to shape definition [1], the use of evolutionary algorithms (EAs) for the optimization process, and the use of surrogate-assisted EAs to reduce the computational cost of the optimization.

Rocket-launched hypersonic flight experiments are rapidly becoming established as a proven cost-effective method for conducting atmospheric flight tests. The HyShot series of flight experiments are an important example of these tests [2,3]. These experiments employ sounding rockets with near-vertical launch angles to boost the experiment into a ballistic trajectory. The trajectory is chosen so that the experiment takes place at the desired

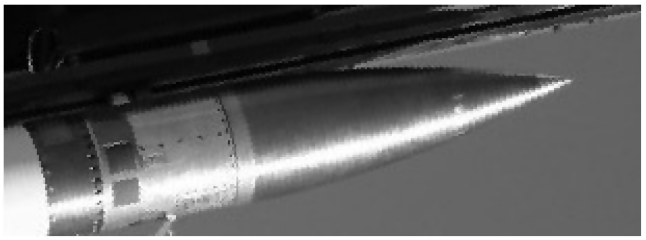

Fig. 1 The 3:1 standard ogive for the HyShot III flight.

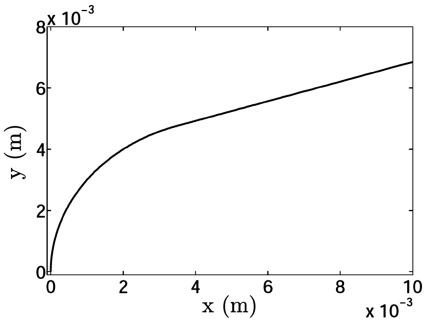

Fig. 2 HyShot's nose-cone tip.

hypersonic Mach number over a range of altitudes (and hence dynamic pressures and Reynolds numbers) on the descent part of the flight. The experiment sits inside a nose cone to protect it from structural and thermal loads during the ascent through the dense parts of the atmosphere. The nose cone is ejected in the upper parts of the atmosphere. The shape of the nose cone has a significant effect on the drag of the vehicle, and hence its trajectory, and is typically a blunted standard ogive. Figure 1 shows a photograph of the standard 3:1 ogive nose cone employed on the HyShot III launch. The overall length of the nose cone is 1.118 m, and the base radius is 0.1785 m. Of particular importance to the present work is the tip region of the nose cone, shown in Fig. 2. It is spherically blunted, with a radius of 0.005 m.

The two nominal ascent-trajectory points considered here are detailed in Table 1 and were chosen somewhat arbitrarily to provide a significant range in both Mach number and Reynolds number. The Reynolds number is based on the length of the nose cone, 1.118 m.

This paper presents a novel approach for shape optimization, applied here to nose cones. To summarize, a reduced PARSEC shape-definition scheme is adopted for the nose-cone shape representation, and an EA is coupled with CFD simulations to find the nose-cone shape with minimal aerodynamic drag force. The problem solved here is thus a single-objective problem, with the objective function being the drag, but the method presented has the flexibility to solve multiobjective problems with constraints more easily than with commonly adopted gradient-based schemes. The shape-representation scheme relies on the nose-cone radius, nose length, gradient of the nose-cone contour at its base, and the base radius as inputs. These parameters have an advantage over those employed by other shape-representation schemes [for example, bezier, B-spline, or nonuniform rational B-spline (NURBS) control points], in that they can be understood to have direct physical influence on the drag. The paper shows results for the reduction of drag at flight Mach numbers 3 and 8 relative to the predicted drag of the actual nose cone used for the HyShot flights [2]. Computation of the drag for the optimum Mach 3 shape at Mach 8 and vice versa highlights the robustness of the designs evolved using such an approach. Furthermore, to reduce the computational time for the process of shape optimization, a surrogate-assisted-optimization approach is introduced. This involves training a radial-basis-function (RBF) network with a collection of CFD-generated snapshots, in which each snapshot is the total drag computed for an arbitrary shape selected using a design-of-experiments approach. This surrogate approximation for the behavior of the nose-cone drag with respect to surface contour is then used in place of many of the required CFD simulations in the EA optimization. The results achieved represent good levels of drag reduction, compared with the fully coupled EA/CFD approach, and are significantly less computationally expensive. A more intense robust-design exercise would be a straightforward extension of the present work, in which the drag of any given shape is optimized at many points along its flight trajectory using the surrogate-assisted model, with each point serving to alter the part of the trajectory that occurs after it.

Table 1 Flowfield conditions for Mach 3.02 and Mach 8.02

Flow parameters	Value (Mach 3.02)	Value (Mach 8.04)
Altitude, km	2.49	82
Angle of attack α, deg	0	0
Freestream Mach number	3.02	8.04
Freestream static pressure, Pa	74789	4.558
Freestream static temperature, K	271.965	217.16
Freestream density, kg m^{-3}	0.95748	7.31e − 05
Freestream Reynolds number	62.465×10^6	15346

II. Optimization

Shape optimization requires a suitable mesh generator and CFD code to predict the flowfield of interest for a given geometry; a suitable shape-representation technique so that the key features of the shape can be accurately represented by a minimal number of parameters, thus minimizing the number of variables to be considered in the optimization; and a suitable optimization algorithm so that the optimized shape is achieved with minimal calls to the CFD code. The particular shape-representation and optimization methods employed here to meet these requirements are discussed after a brief review of previous approaches. They are outlined to a sufficient level of detail to enable the high-speed-vehicle optimization practitioner to implement the approach. The details of the CFD method and mesh generation are provided in Sec. III.

A. Previous Optimization Approaches

The optimization of high-speed-vehicle geometries has had a very long history that precedes modern numerical approaches. Newton [4] employed calculus to choose the axisymmetric nose-cone shape, of specified aspect ratio and at given freestream conditions, that has minimum wave drag. His approach made many simplifying assumptions that, surprisingly, result in reasonably accurate drag predictions at hypersonic speeds. In the late 1950s, this was recognized (see [5]) and applied to minimum-drag supersonic and hypersonic nose-cone design {for example, Gonor (1960) [6]}. The results are typically of the same order of accuracy as solutions to the Euler equations [5]. Around the same time, nose-cone optimization for minimum drag using the Euler equations was performed [7].

The application of optimization techniques to aerospace vehicles in general dates back a little earlier, with Lighthill (1945) [8] employing conformal mapping for the optimal design of two-dimensional airfoils. In recent times, many approaches haven been investigated for computationally efficient shape optimization techniques for aerospace applications. These are briefly discussed next. The reader is referred to the literature for the relevant details. In terms of shape representation, the common types include PARSEC representation [9,10], B-splines [11,12], beziers [13], and NURBS [14]. These shape-representation schemes are coupled with a variety of optimization methods such as genetic algorithms (GAs), EAs, simulated annealing, gradient-based methods, and adjoint formulations (based on control theory). In the context of airfoil shape optimization, EAs [11], GAs [10], and hybrids [15] were used for single-objective optimization, whereas multiobjective formulations were solved using nondominated sorting GAs [13] and multiobjective GAs [12]. PARSEC shape representation is particularly attractive because the design variables (the nose-cone radius, nose length, slope at the base and the base radius) have a direct influence on drag, unlike the control points of beziers, B-splines, or NURBS.

Population-based, zero-order, elitist optimization methods such as GAs and EAs are quite attractive for such classes of problems, because they do not rely on continuity of the objective and constraint functions or their gradients and are known to be effective for nonlinear problems. However, both genetic- and evolutionary-algorithm methods require a significant number of evaluations of candidate designs before convergence. Furthermore, they require a number of user inputs on crossover and mutation probabilities, types of crossover, population, and generation details.

To reduce the computational time for such shape optimization problems, reduced-order models are usually embedded within GAs or EAs. Furthermore, for multipoint and robust-design problems, surrogate assistance is necessary, because for every candidate design, its performance over a range of operating points needs to be computed, which adds to the computational cost. To provide some examples, a multipoint nose shape optimization for a space launcher was performed [16] using a surrogate-assisted-optimization model; the design of robust missile geometries has recently been reported using Pareto-optimal genetic algorithms [17], and EAs were embedded with artificial neural network models for the optimization of a fixed-wing reusable launch vehicle [18]. However, GA and EAs in their native form are not capable of handling constraint functions. Furthermore, for multiobjective problems, such algorithms deliver a set of nondominated solutions and consider diversity solely in the objective space. This in turn eliminates the possibility of the existence of solutions that are different in the variable space and yet close in the objective space.

Gradient-based optimization methods have had limited success for such problems, because they become computationally expensive, due to gradient computations for problems with a large number of variables. Furthermore, because they are point-improvement algorithms, the entire set of Pareto-optimal solutions cannot be generated, unlike population-based approaches such as GAs and EAs. The presence of constraints is also known to influence the performance, due to inherent problems with penalty-function methods.

B. Overview of the Approach Employed Here

In this paper, we describe an evolutionary algorithm that has been used elsewhere [19] but is applied to hypersonic problems for the first time here. It is similar to the nondominated sorting genetic algorithm NSGA-II [20] but has explicit means to maintain variable diversity. The nose-cone shape is represented using a reduced PARSEC formulation that was found to provide better control for shape optimization of airfoils [1]. ANSYS CFX is used as the core CFD solver, which was extensively validated for low- and high-speed applications. As for the surrogate-assisted-optimization model, a radial-basis-function model was created using the points from an orthogonal array that was then used in lieu of CFD computations within EAs. The test cases include a single-point optimum shape design at Mach 3 and Mach 8 at the same flight conditions as HyShot, with constraints being a minimum nose-cone-tip radius and a fixed nose-cone length and base radius identical to HyShot. These constraints were imposed because the emphasis here is on drag reduction via *shape* optimization, rather than by simply making the cone longer and sharper. The robustness of the single-point designs are established by computing the performance of the optimum Mach 3 shape at Mach 8 and vice versa. The study reports significant savings in drag reduction when compared with the existing HyShot design and also highlights the benefits of a surrogate-assisted-optimization approach for a more elaborate robust-design exercise.

A variety of nose-cone shape-representation schemes exist today that use a different number of variables and different mathematical functions linking the variables; however, an ideal shape-representation scheme should possess the following features:

1) It should have the flexibility to explore the entire search space, including nonconventional shapes.

2) It should require a minimum number of variables for shape definition, because large numbers of variables result in enormous optimization problems.

3) The shape-representation scheme should avoid the generation of sharp discontinuities in surface gradients.

4) The variables should be related to the aerodynamic performance that is being optimized.

Once a shape-representation scheme is adopted, the number of variables for the optimization problem is fixed. To use these variables effectively in any optimization problem, the upper and lower bounds of the variables must be assigned. Inverse shape-fitting employing an initial guess (for example, the actual HyShot nose cone) can be used to get an initial estimate of the variables, and an approximate percentage can be used to decide the variable bounds. In this study, the PARSEC [10] representation scheme is used to define the nose-cone geometries, because it requires only four variables and allows the possibility of better control over the shape during the course of optimization. The details of PARSEC representation and the bounds for its variables used in this work are presented next.

C. Details on the Approach Employed Here

1. *PARSEC Shape Representation*

Unlike common engineering design optimization problems in which the number and nature of the variables are fixed, the number of variables of a shape optimization problem are influenced by the choice of the shape-representation scheme. The PARSEC [1] representation is particularly attractive because it uses a small number of design variables, all of which are related to some properties of the shape. The variables here are the length and base diameter of the nose cone, the tip radius, and the gradient of the surface at the trailing edge. Our reduced PARSEC representation then parametrizes the nose-cone surface using polynomials in coordinates X and Z, as shown in Eq. (1), in which a_n are real coefficients.

$$Z = \sum_{n=1}^{4} a_n X^{n-\frac{1}{2}} \tag{1}$$

In the present work, we constrained all four variables to a length of 1.118 m, a base diameter of 357 mm, a tip radius of 5 mm, and a trailing-edge gradient of 0. The optimization problem is then truly a drag minimization due to shape optimization, rather than by, for example, making the body longer and more slender. The optimization process thus seeks the set of coefficients a_1 to a_4 that specify the optimal shape. Constraints were placed on their bounds to avoid complex (for example, wavy) shapes being produced. The initial set was obtained using an inverse fit to the standard blunted ogive used for the nose cone in the HyShot II flight test.

2. *Evolutionary Algorithm*

The particular evolutionary algorithm described here is summarized in pseudocode in Algorithm 1 and follows the broad steps of initialize, selection, crossover and mutation, ranking, and reduction. These steps are detailed next.

Algorithm 1 Top level of the evolutionary algorithm

Require $N_G > 1$ (number of generations)
Require $M > 0$ (population size)
$P_1 =$ initialize( )
Evaluate (P_1)
for $i = 2$ to N do
  Rank (P_{i-1})
  repeat
    $p1, p2 =$ select(P_{i-1})
    $c1, c2 =$ crossover($p1, p2$)
    Mutate ($c1$)
    Mutate ($c2$)
    Add $c1, c2$ to C_{i-1}
  until C_{i-1} has M children
  Evaluate ($C_{i-1}, \mathcal{S}$)
  $P_i =$ reduce($P_{i-1} + C_{i-1}$)
end for

A. Initialize. All the solutions to the nose-cone shape in the population are initialized by individual variables (that is, individual coefficients a_1 and so on), as given in Eq. (2).

$$x_i = \underline{x}_i + \mathcal{U}[0, 1](\overline{x_i} - \underline{x}_i) \qquad 1 \le i \le n \tag{2}$$

where x_i denotes the initialized coefficient, and $\mathcal{U}[0, 1]$ is a uniform random number between 0 and 1.

B. Selection. The procedure for selection of parents is the same as that of NSGA-II [20]. Two shuffled lists of individuals (1 to M) are created. From each list, four individuals are chosen sequentially. Two parents are chosen from these four individuals using the process of binary tournament. Binary tournament between two individuals $\mathbf{x}^1$ and $\mathbf{x}^2$ is performed as follows:

1) If $\mathbf{x}^1$ is feasible (satisfies all the constraints) and $\mathbf{x}^2$ is infeasible (violates one or more constraints), $\mathbf{x}^1$ is selected.

2) If both $\mathbf{x}^1$ and $\mathbf{x}^2$ are not feasible, the one having the least degree of violation of the constraint that is violated to the greatest degree is selected.

3) If both $\mathbf{x}^1$ and $\mathbf{x}^2$ are feasible and $\mathbf{x}^1$ dominates $\mathbf{x}^2$, $\mathbf{x}^1$ is selected and vice versa.

4) If both $\mathbf{x}^1$ and $\mathbf{x}^2$ are feasible and none dominated the other, a random selection is made between $\mathbf{x}^1$ and $\mathbf{x}^2$.

C. Crossover and Mutation. We used simulated binary crossover for the real variables, as adapted in NSGA-II, to create two children from a pair of parents. The offsprings $\mathbf{y}^1$ and $\mathbf{y}^2$ are created from parents $\mathbf{x}^1$ and $\mathbf{x}^2$, as shown in Eq. (3) [21].

$$\begin{aligned} y_i^1 &= 0.5[(1 + \beta_{q_i})x_i^1 + (1 - \beta_{q_i})x_i^2] \\ y_i^2 &= 0.5[(1 - \beta_{q_i})x_i^1 + (1 + \beta_{q_i})x_i^2] \end{aligned} \tag{3}$$

where β_{q_i} is calculated as

$$\beta_{q_i} = \begin{cases} (2u_i)^{1/\eta_c+1} & \text{if } u_i \le 0.5 \\ \left(\frac{1}{2(1-u_i)}\right)^{1/\eta_c+1} & \text{if } u_i > 0.5 \end{cases} \tag{4}$$

where u_i is the uniform random number in the range [0, 1), and η_c is the user-defined parameter called *distribution index for crossover*. The mutation operator used is the polynomial mutation operator defined by Deb and Agrawal [21]. Each variable of $\mathbf{y}$ is obtained from a corresponding variable of $\mathbf{x}$, as given in Eq. (5) [21].

$$y_i = x_i + (\overline{x_i} - \underline{x}_i)\bar{\delta}_i \tag{5}$$

where $\bar{\delta}_i$ is calculated as

$$\bar{\delta}_i = \begin{cases} (2r_i)^{1/(\eta_m+1)} - 1 & \text{if } r_i < 0.5 \\ 1 - [2(1 - r_i)]^{1/(\eta_m+1)} & \text{if } r_i \ge 0.5 \end{cases} \tag{6}$$

where r_i is the uniform random number in the range [0, 1), and η_m is the user-defined parameter called *distribution index for mutation*.

Table 2 Grid sensitivity statistics at $M_\infty = 8.04$

Grid	x	y	Nodes	Drag force, N
Grid 1	75	225	16875	6.156
Grid 2	150	450	67500	6.120
Grid 3	300	900	270000	6.118

D. Ranking. Ranking of the solution involves ranking feasible and infeasible solutions separately. Feasible solutions are first sorted using the method of nondominated sorting to generate fronts of nondominated solutions. Solutions within each front are ranked based on the decreasing crowding distance. Infeasible solutions are ranked based on increasing value of the maximum violated constraint.

E. Reduction. The reduction procedure for retaining M solutions for the next generation from a set of $2M$ solutions (parent and offspring population) uses the ranks obtained from the ranking procedure. This process, unlike NSGA-II, explicitly considers the diversity of solutions in both the objective and the variable space, as follows:

1) If the feasible solutions are more than M, M solutions are selected in the order of nondominated fronts and decreasing crowding distance in each front.

2) If the feasible solutions are less than or equal to M,

a) All the feasible solutions are selected in the order of nondominated fronts and decreasing crowding distance in each front.

b) Remaining solutions are selected from infeasible solutions in the order of minimum value of maximum constraint violation.

3. *Surrogate-Assisted Optimization*

For realistic CFD/optimization problems, the most primitive forms of EAs are often prohibitive because of the need to perform CFD calculations for each shape generated in the process. To reduce computational time for such an exercise, surrogate approximation functions are generated from a selection of CFD solutions and used to replace many of the calls to the CFD solver. In the present work, the surrogate approximation function is a representation of the nose-cone drag as a function of the variables used to define the surface shape. It was generated by considering a selection of CFD snapshots (for example, 164 in the Mach 3 case), which were chosen with a design-of-experiments approach. The surrogate model is then a one-shot RBF neural network trained from these snapshots.

The surrogate-assisted optimization used here is a population-based approach that starts with an initial set of population of candidate solutions and evolves them over a number of generations to finally arrive at a set of desired solutions. The algorithm performs actual evaluations of objectives and constraints for all the members of the initial population and periodically evaluates all the members of

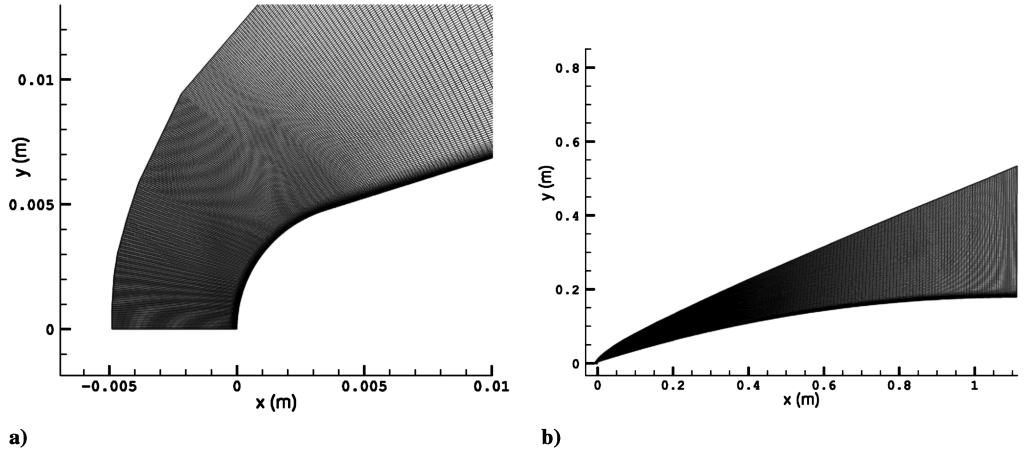

Fig. 3 Mesh around a) nose-cone tip and b) nose cone.

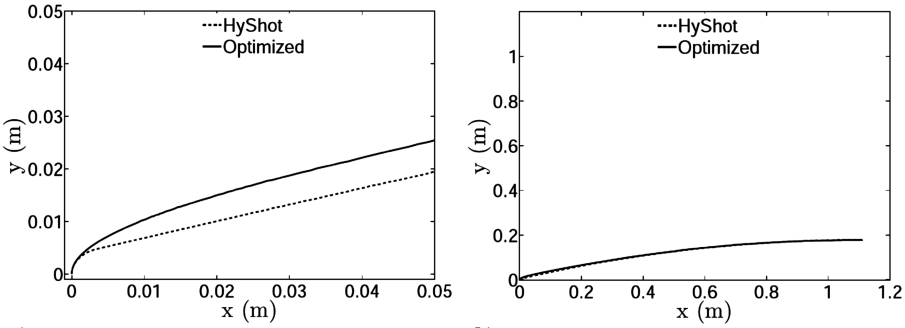

Fig. 4 Optimized nose-cone shape representation for Mach 3: a) tip and b) entire body.

the population after every S generations. An external archive of the unique solutions evaluated using actual analysis is maintained to train the RBF model, which is then used in lieu of actual analysis for the next S generations. To ensure the prediction accuracy of the RBF surrogate model, a candidate solution is only approximated if at least one candidate solution in the archive exists in the vicinity (based on a user-defined distance threshold).

III. Computational Fluid Dynamics

A. Flowfield Simulations

The purpose of this paper is to demonstrate the reduction in drag that is achievable through shape optimization employing the EA already described and to demonstrate the savings in computational time achieved by employing a surrogate-assisted approach. To this end, the choice of CFD code is not critical; however, the code should at least be suitable for the class of flows considered, which are supersonic and hypersonic in this case. We have elected to use the commercial CFD code ANSYS CFX [22], with which validation work was performed for supersonic and hypersonic flow conditions [23–25]. CFX is a fully implicit, conservative, finite volume, Reynolds-averaged Navier–Stokes CFD code. Turbulence was modeled using a k-ω-based shear stress transport model, with an assumption of 1% turbulent intensity in the inflow conditions. This model was selected because it has demonstrated superior performance for various validation cases [26,27]. The shear stress transport model, like other eddy-viscosity models, exhibits laminar-to-turbulent transition behavior: on a configuration such as a flat plate or the nose cone investigated here, the eddy viscosity production is initially small, and thus the boundary layer is initially laminar. As the boundary layer develops, the eddy viscosity increases. If it exceeds the viscosity, turbulence effectively starts and transition has effectively occurred. This depends on the inflow conditions and for low Reynolds numbers will require large flow lengths to occur. As will be seen in the results presented in this paper, transition to turbulence occurs just downstream of the tip region of the nose cone for the low-altitude high Reynolds number $M_\infty = 3.02$ case, whereas for the high-altitude low Reynolds number $M_\infty = 8.04$ case, transition does not occur at all. The complete set of partial differential equations was solved using the additive-correction [28] algebraic-multigrid accelerated incomplete-lower/upper factorization technique.

The thermodynamics of the fluid were modeled by representing the air as a thermally perfect single species. For all cases, the adiabatic wall condition was employed. Temporal convergence was assumed once the global rms values of the residuals of *all* the equations have reduced by four orders of magnitude.

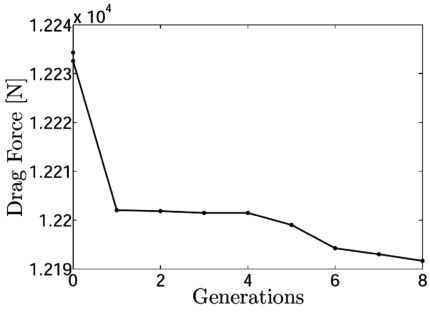

Fig. 5 Progress plot of Mach 3 optimization.

B. Grid Generation and Sensitivity

For grid generation, the commercial mesh generator ICEM-CFD was used to automatically generate meshes for each shape variation. A structured C-grid topology was used around the nose cone, comprising 450×150 nodes in the chordwise and normal-to-surface directions, respectively. The quality of the $2 \times 2 \times 2$ determinant of the mesh is assured to be more than 0.9 in every case. To adequately resolve boundary layers and thus the contribution from viscous drag, the first node distance is maintained at $1E-6m$ from the wall. The $M_\infty = 3.02$ and 8.04 cases have similar grids to those shown in Fig. 3. The grid spacing is the same in both cases. For $M_\infty = 3.02$, the y^+ value for the first node from the wall varied from approximately 2 at the nose to 16 at the trailing edge, whereas for $M_\infty = 8.04$, the y^+ value varied from approximately 0.004 at the nose to 0.011 at the trailing edge. In the latter case, the y^+ value is so low because, as will be seen later, the boundary layer is so thick that it merges with the bow shock. In both cases, the resolution of the boundary layer is very good.

Grid sensitivity studies of the influence of the grid on the drag were performed on a particular nose cone that was obtained from an inverse fit to the HyShot geometry, at both the Mach 3 and 8 flow conditions. A grid-refinement factor of 2 was maintained for each successive refinement, and a comparison for Mach 8 is presented in Table 2. Here, x and y represent the number of grid points on the normal-to-surface and chordwise directions, respectively. The change in drag-force value between grid 2 and grid 3 was 0.03%. To estimate the level of uncertainty in the simulated drag due to mesh dependence, the grid convergence index (GCI) was computed for changes in the drag between grids 1 and 2 and 2 and 3, following the method recommended in [29]. For Mach 3, the analysis yields GCI = 0.028% for the former and 0.007% for the latter. For Mach 8, the analysis yields GCI = 0.042% for the former and 0.002% for the

Table 3 Comparative drag results with HyShot for Mach 3

Nose Cone	Inviscid drag, kN	Viscous drag, kN	Total drag, kN	Total C_D
HyShot	11.56	0.80	12.36	0.2601
Optimized shape	11.43	0.76	12.19	0.2565

latter. In other words, the level of uncertainty due to mesh dependence in the simulated drag by using grid 2 is less than 0.01%, and therefore grid 2 was chosen for all the simulations in the optimization studies.

IV. Results and Discussion

In the preceding manner, three collections of CFD simulations were performed for each flight condition: a simulation for the original HyShot standard ogive/cylinder, to provide baseline data; a shape optimization series of simulations in which the CFD code was called to calculate the drag for every generation; and a surrogate-assisted shape optimization series. The results of these are presented for each Mach number. The performance of the optimized shapes at each Mach number is computed and presented, to assess the off-design performance (robustness) of the shapes.

A. $M_\infty = 3.02$

As described earlier, the original HyShot ascent geometry consisted of a spherical 5-mm-radius nose followed by a standard ogive/cylinder combination. This results in a particular flowfield that is described next and that is fundamentally different from that of the optimized shape. To assist the discussion that follows, Fig. 4

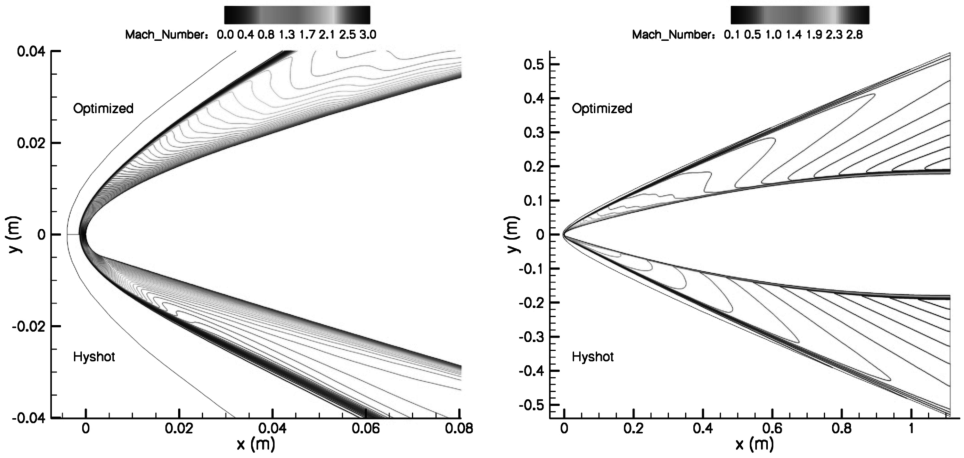

a) b)

Fig. 6 Mach Contours of HyShot (lower) and optimized (upper) shapes at $M_\infty = 3.02$: a) nose-cone tip and b) nose cone.

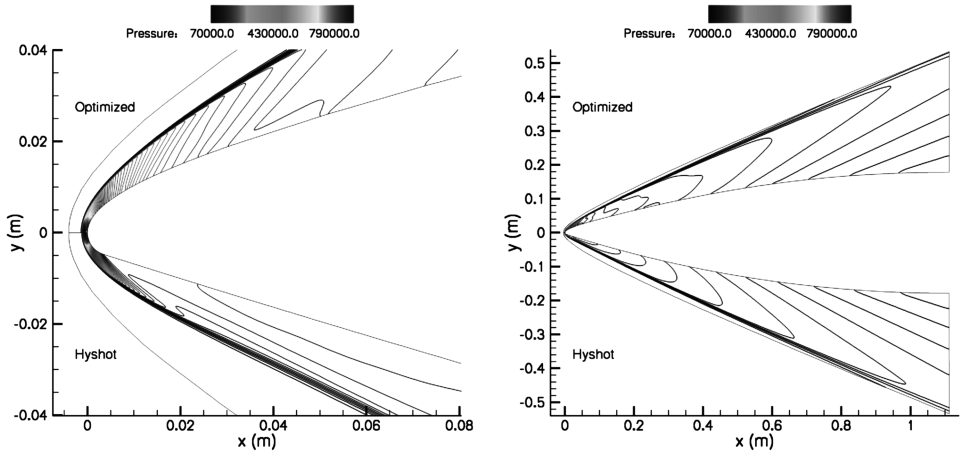

a) b)

Fig. 7 Pressure contours of HyShot (lower) and optimized (upper) shapes at $M_\infty = 3.02$: a) nose-cone tip and b) nose cone.

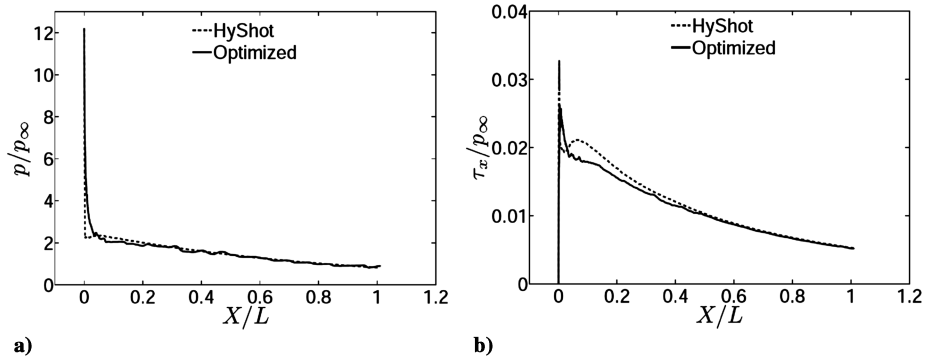

a) b)

Fig. 8 Surface distribution on nose cone for Mach 3: a) pressure distribution and b) wall shear stress.

Table 4 Comparative study between CFD and surrogate-assisted optimization for Mach 3

Model	Inviscid drag, kN	Viscous drag, kN	Total drag, kN	Total C_D	Inviscid drag reduction, %	Viscous drag reduction, %	Total drag reduction, %
HyShot	11.56	0.80	12.36	0.2601	——	——	——
CFD optimization	11.43	0.76	12.19	0.2565	1.13	5.26	1.39
Surrogate-assisted optimization	11.45	0.76	12.21	0.2569	0.87	5.26	1.21

compares the original shape (upper part of the figure) with the optimized shape (non-surrogate-assisted). The comparison is striking. The original shape has a discontinuous curvature of the contour at the end of the spherical cap. In comparison, for a *lower* drag and for the same overall length and base radius, the optimized shape has continuous curvature throughout and is *less* slender than the original shape near the nose.

The EA optimization process employed here was taken to eight generations, involving 200 individual CFD simulations, and the progress of this process with regard to absolute drag force is plotted in Fig. 5. The figure indicates that the first generation of shapes has produced the most reduction in drag. By taking the process to eight generations, more reduction is achieved, and the figure suggests that further reduction is possible with further iterations of the process (with increased computational expense, of course). Table 3 provides the quantitative drag-reduction results. At this Mach number, the standard shape has a drag coefficient (with respect to the base area) of 0.2601, of which 6.5% is composed of viscous drag. The shape optimization process generated a surface contour with a drag coefficient of 0.2565 (a reduction of 1.39%).

To understand how this drag reduction was achieved and why the optimized shape that achieves this reduction is *less* slender, consider the Mach number and static pressure comparisons for the two shapes that are presented in Figs. 6 and 7 and the surface pressure and surface shear stress distribution comparisons in Fig. 8. The key to the drag reduction is the nose region. In the standard shape, with the discontinuous change from a spherical tip to the ogive, that change in surface gradient initially expands the flow further than the optimized shape, but *overexpands* it. A relatively strong compression then corrects this situation, with the result that the local surface pressure is higher for the standard shape than the optimized shape downstream of the discontinuity, over a considerable distance. The effect of this away from the surface is evident in Figs. 6 and 7. The wall shear stress for the standard shape shows an initial rapid decrease along the body, followed quickly by a rise due to transition to turbulence. This was observed to occur at the streamwise location (x/L of approximately 0.06), for which the turbulent kinetic energy rises suddenly. The optimized shape is contoured such that the flow does not expand too quickly, and the pressure field both on and off the surface is better-behaved, with lower overall pressure and lower integrated inviscid

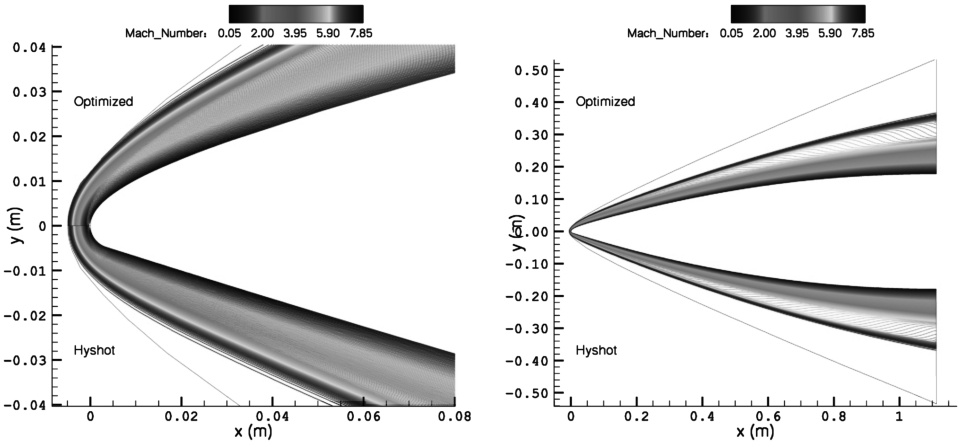

Fig. 9 Mach contours of HyShot at $M_\infty = 8.04$: a) tip and b) entire body.

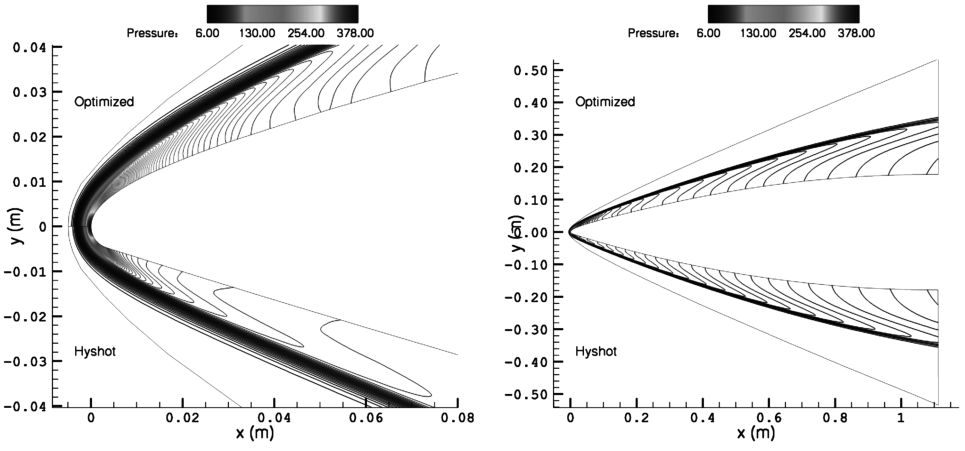

Fig. 10 Pressure contours of HyShot at $M_\infty = 8.04$: a) tip and b) entire body.

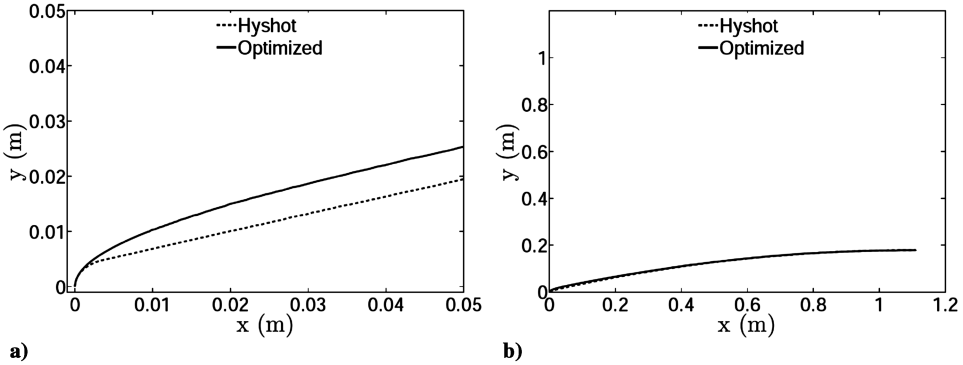

Fig. 11 Optimized nose-cone shape representation for Mach 8: a) tip and b) entire body.

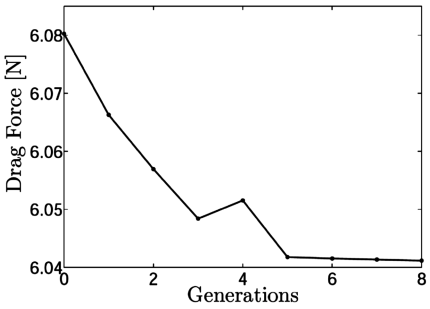

Fig. 12 Progress plot of Mach 8 optimization.

drag, as a result. The effect on the wall shear stress is even more pronounced, as shown in Fig. 8b. The rise in turbulent kinetic energy at transition for the optimized case is delayed until further downstream (x/L of approximately 0.15), and the wall shear stress no longer rises at transition, but rather slows its rate of decay. As a result, the optimization process had a greater effect on the viscous drag than on the inviscid drag. This is summarized in Table 4: the shape optimization has decreased the inviscid drag (the dominant drag component) by 1.13%, and the viscous drag was reduced by 5.26%.

The shape generated by the surrogate-assisted-optimization process is very similar to the preceding result and is not shown here. However, Table 4 shows that the surrogate-assisted shape represents an overall drag reduction from the standard shape of 1.21%, with the greatest effect again for the viscous drag. This is almost as good (87%) as the non-surrogate-assisted reduction and was achieved with only 164 CFD calls (an 18% saving in computational expense). This illustrates the power of the approach described here: the drag savings for the case considered here are modest (but still significant), but the potential for achieving these reductions with significant reduction in computational expense via the surrogate-assisted approach is large. This opens up the possibility for the optimization of more complex configurations that would otherwise be too expensive to consider attempting.

B. $M_\infty = 8.04$

Following an identical procedure, the Mach 8 trajectory point has also been considered here. The results are qualitatively similar to the Mach 3 results, as will be seen next. However, the nature of the flowfields involved are fundamentally different. Figure 9 compares Mach number contours for the standard and optimized shapes, and Fig. 10 gives the pressure-contour comparison. The optimized shape is shown in Fig. 11 and is similar to the Mach 3 case, avoiding discontinuous changes in curvature. Figure 12 plots the optimization progress and suggests that the shape arrived at would not be significantly improved with further generation iterations. The actual flow-parameter-contour distributions are *not* typical of those usually encountered for supersonic/hypersonic flow; for example, there is no distinct subsonic region completely filling the space between the nose and the normal part of the bow shock, followed by expansion to supersonic flow. Instead, a large subsonic layer follows the nose-cone contour from tip to tail.

The reason for this large subsonic layer is the very low density at the altitude considered for this case. Viscous effects dominate the flow to the extent that over much of the region simulated, the bow shock and boundary layer are fully merged. Furthermore, inspection of the distribution of turbulent kinetic energy along the body (not shown here) indicates that transition has *not* occurred for this low Reynolds number case. This was confirmed with a separate fully laminar (that is, with no turbulence model employed) calculation, and the two results agreed extremely well: the difference in viscous drag between the turbulent and fully laminar calculations was 0.03%. As a result, the distribution of wall shear stress shown in Figure 13b does not display the structure associated with transition that was the case for the Mach 3 results. Figure 14 gives Knudsen number contours for the standard shape case and suggests that because much of the flowfield has values of the order of 1, that molecular collision mean free paths are not small relative to the scale of the nose cone and that rarefaction effects are likely to be important. CFX is a *continuum* code, and so the actual quantitative data presented here should be treated with some caution. To provide an independent check on the results without resorting to direct simulation Monte Carlo methods, we repeated this calculation with a completely different code, the *density-based* continuum code CFD $++$ [30]. The results from that

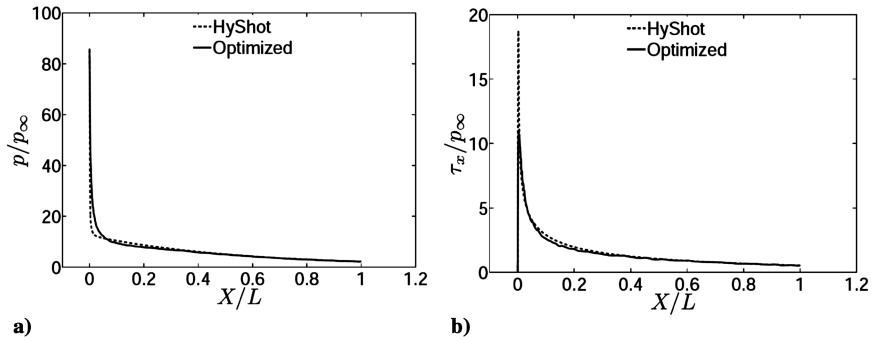

Fig. 13 Surface distribution on nose cone at Mach 8: a) pressure distribution and b) wall shear.

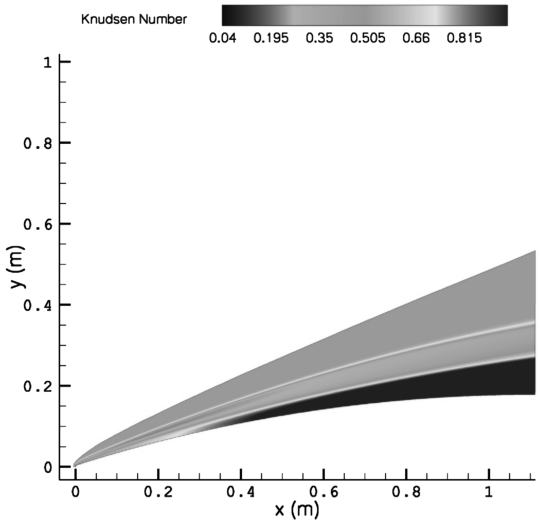

Fig. 14 Knudsen number for Mach 8 flow conditions.

calculation were in good agreement with the CFX simulation here and yielded a drag within 1.7% of the CFX value. This gives some confidence in the present Mach 8 results. However, even if they are in error due to low-density effects, the error is systematic and the phenomena present in this case provide an opportunity to further test the optimization procedure and to assess the robustness of the optimized shape.

Tables 5 and 6 summarize the Mach 8 results. More than half of the drag is due to viscous effects, and the overall drag coefficient is 20% higher than in the Mach 3 case. The viscous effects have had a damping effect on the overexpansion/compression effect of the standard geometry, so that the surface pressure and shear stress distribution comparisons (Fig. 13) for each shape are more similar than for the higher-density Mach 3 case. The levels of reduction in inviscid and viscous drag are similar for the Mach 8 case.

For this case, the surrogate-assisted process has also resulted in drag reduction, but not as successfully as the non-surrogate-assisted approach. However, the reduction in computational expense is again significant, with the number of calls to the CFD solver reduced from 200 to 178 (a reduction of 11%).

C. Off-Design Performance (Robustness) of the Optimized Shapes

In the preceding results, nose-cone shapes were independently optimized for the Mach 3 and Mach 8 conditions. Although requiring *considerably* greater computational expense, it is a simple matter to extend that process to arrive at a *robust* shape that achieves the optimum drag-coefficient reduction over the entire Mach number range considered. The absolute drag force, on the other hand, is dominated for a HyShot-like ascent trajectory by the lower altitudes, despite their lower Mach numbers, and so the best design for the entire ascent is likely to be the low-altitude design. On the other hand, acceleration in a flatter trajectory would elevate the importance of a robust-design optimization. Again, this is a simple extension of the current approach.

To assess the robustness achieved here with regard to the drag coefficient, CFD simulations were produced for the Mach 3 optimized shape at the Mach 8 condition and vice versa. The results are presented in Table 7 and show that the off-design shape performs nearly as well as the on-design shape at the relevant flight condition. In other words, irrespective of the Mach number and irrespective of the importance of viscous effects, by improving the surface contour so that curvature discontinuities are removed, significant drag reduction can be achieved. The case considered here is relatively simple: more significant improvements in aerodynamic efficiency, accompanied by reduced computational expense due to the implementation of surrogate assistance, would be expected for more complex configurations.

V. Conclusions

The major conclusions from the study can be summarized as follows. First, a PARSEC shape-representation scheme was introduced in the context of hypersonic vehicles (specifically, hypersonic nose cones). This provided adequate flexibility when compared with other shape representations commonly adopted for nose-cone shape representation. This shape representation required the use of only four geometric variables: the overall length, overall base radius, nose-tip radius, and trailing-edge gradient. The

Table 5 Comparative study with HyShot for Mach 8

Nose Cone	Inviscid drag, N	Viscous drag, N	Total drag, N	Total C_D
HyShot	2.579	3.582	6.161	0.3001
Optimized shape	2.524	3.516	6.040	0.2942

Table 6 Comparative study between CFD and surrogate-assisted optimization (SAO) for Mach 8

Model	Inviscid drag, N	Viscous drag, N	Total drag, N	Total C_D	Inviscid drag reduction, %	Viscous drag reduction, %	Total drag reduction, %
HyShot	2.579	3.582	6.161	0.3001	——	——	——
CFD optimization	2.524	3.516	6.040	0.2942	2.17	1.87	1.96
Surrogate-assisted optimization	2.570	3.542	6.112	0.2977	0.35	1.12	0.80

Table 7 Comparative study between the HyShot and optimized shape design variables for Mach 8 and Mach 3

Nose cone	Freestream Mach number	C_D	Drag reduction, %
HyShot	3.02	**0.2601**	——
Best shape ($M_\infty = 3.02$)	3.02	0.2565	1.39
Best shape ($M_\infty = 8.04$)	3.02	0.2571	1.13
Hyshot	8.04	**0.3001**	——
Best shape ($M_\infty = 8.04$)	8.04	0.2942	1.96
Best shape ($M_\infty = 3.02$)	8.04	0.2945	1.86

particular shape of the surface was then specified with a polynomial expansion, and the optimization sought the values of the coefficients in the expansion. In this study, the length and radius were fixed, so that the drag reduction was performed on the basis of shape only. Second, using our EA implementation, drag reductions of 1.39 and 1.96% due to shape optimization at Mach 3 (low altitude) and Mach 8 (high altitude), respectively, were achieved relative to the original HyShot nose cone. The Mach 3 flowfield was inviscid-dominated, whereas the high-altitude Mach 8 flowfield was viscous-dominated. Third, our surrogate-assisted method, using a one-shot radial-basis-function network trained from design-of-experiments-selected CFD snapshots of the flow, achieved nearly the same drag reduction as the non-surrogate-assisted approach, particularly at Mach 3, with the advantage of significant savings in computational expense. This is expected to yield improvements in design efficiencies (aerodynamic performance compared with computational expense) for complex geometries. Finally, for the present case, the improvement in shape by removing curvature discontinuities leads to a robust design with respect to both altitude and Mach number. Extension of the present algorithm to full robust-design optimization is a trivial process.

References

[1] Ray, T., and Tsai, H. M., "Swarm Algorithm for Single- and Multiobjective Airfoil Design Optimisation," *AIAA Journal*, Vol. 42, No. 2, 2004, pp. 366–373.

[2] Boyce, R. R., Frost, M., and Paull, A., "Combustor and Nozzle CFD Calculations for the HyShot Scramjet Flight Experiment," *Computational Fluid Dynamics Journal*, Vol. 12, No. 2, 2003, pp. 216–226.

[3] Boyce, R. R., Gerard, S., and Paull, A., "The HyShot Scramjet Flight Experiment—Flight Data and CFD Calculations Compared," AIAA Paper 2003-7029, 2003.

[4] Newton, I., *Philosophiae Naturalis Principia Mathematica*, T. T. and J. Tegg, London, 1833.

[5] Kraiko, A. N., Ye Pudovikov, D., P'Yankov, K. S, and Tillyayeva, N. I., "Axisymmetric Nose Shapes of Specified Aspect Ratio, Optimum or Close to Optimum with Respect to Wave Drag," *Journal of Applied Mathematics and Mechanics*, Vol. 67, No. 5, 2003, pp. 703–730. doi:10.1016/S0021-8928(03)90043-8

[6] Gonor, A. L., "Determination of the Shape of Bodies of Minimum Drag at High Supersonic Velocities," *Prikladnaya Matematika i Mekhanika*, Vol. 24, No. 6, 1960, pp. 1073–1078.

[7] Chernyi, G. G., "Supersonic Flow Past a Profile Close to a Wedge," *Gas Dynamics: Selected Works*, Vol. 1, edited by A. N. Kraiko and A. N. Sekundov, Fizmatlit, Moscow, 2000.

[8] Lighthill, M. J., "A New Method of Two-Dimensional Aerodynamic Design," NACA Rept. 2112, 1945.

[9] Ginnakoglou, K. C., "Design of Optimal Aerodynamic Shapes Using Stochastic Optimisation Method and Computational Intelligence," *Progress in Aerospace Sciences*, Vol. 38, 2002, pp. 43–76. doi:10.1016/S0376-0421(01)00019-7

[10] Holst, T. L., and Pulliam, T. H., "Aerodynamic Shape Optimization Using a Real-Number-Encoded GA," AIAA Paper 2001-2473, 2001.

[11] DeFalco, I., Della Cjoppa, A., Iazzetta, A., and Tarantino, E., "Evolutionary Algorithms for Airfoil Design," *International Journal of Computational Fluid Dynamics*, Vol. 11, Nos. 1–2, 1998, pp. 51–77. doi:10.1080/10618569808940865

[12] Vicini, A., and Quagliarella, D., "Inverse and Direct Airfoil Design Using a Multiobjective Genetic Algorithm," *AIAA Journal*, Vol. 35, No. 9, 1997, pp. 1499–1505.

[13] Marco, N., Desideri, J., and Lanteri, S., "Multiobjective Optimisation in CFD by Genetic Algorithms," Institut National de Recherche en Informatique et en Automatique, Rept. 3686, Le Chesnay, France1999.

[14] Lepine, J., Guibault, F., and Trepanier, J. Y., "Optimized Nonuniform Rational B-Spline Geometrical Representation for Aerodynamics Design of Wings," *AIAA Journal*, Vol. 39, No. 11, 2001, pp. 2033–204.

[15] Quagliarella, D., and Vicini, A., "Combining Genetic Algorithms and Gradient Based Optimisation Technique," *Genetic Algorithms in Engineering and Computer Science*, edited by Winter, G., Periaux, J., Galan, M., and Cuesta, P., Wiley, Chichester, England, U.K., 1995.

[16] Jae-Woo Lee, Byung-Young Min, and Yung-Hwan Byun, "Multipoint Nose Cone Optimization of Space Launcher Using Response Surface Method," *Journal of Spacecraft and Rockets*, Vol. 43, No. 1, 2006, pp. 137–146.

[17] Anderson, M. B., Burkhalter, J. E., and Jenkins, R. M., "Missile Aerodynamic Shape Optimization Using Genetic Algorithms," *Journal of Spacecraft and Rockets*, Vol. 37, No. 5, 2000, pp. 663–669.

[18] Chiba, K., Obayashi, S., Nakahashi, K., Giotis, A. P., and Giannakoglou, K. C., "Design Optimisation of the Wing Shape for the RLV Booster Stage Using Evolutionary Algorithms and Navier–Stokes Computations on Unstructured Grids," *Proceedings of the Fifth Conference on Evolutionary Methods for Design, Optimization and Control with Applications to Industrial Problems (EUROGEN 2003)*, 2003.

[19] Ray, T., and Smith, W., "A Surrogate Assisted Parallel Multiobjective Evolutionary Algorithm for Robust Engineering Design," *Engineering Optimization*, Vol. 38, No. 8, 2006, pp. 997–1011. doi:10.1080/03052150600882538

[20] Deb, K., Agrawal, S., Pratab, A., and Meyarivan, T., "A Fast Elitist Nondominated Sorting Genetic Algorithm for Multi Objective Optimization: NSGA-2," *Parallel Problem Solving from Nature*, edited by Schoenauer, M., Springer–Verlag, New York, 2000, pp. 849–858.

[21] Deb, K., and Agrawal, R. B., "Simulated Binary Crossover for Continuous Search Space," *Complex Systems*, Vol. 9, 1995, pp. 115–148.

[22] ANSYS CFX, Software Package, Ver. 11.0, ANSYS, Inc., Canonsburg, PA, 2007.

[23] Jagadeesh, G., Dhinagaran, R., Haridoss, K., and Reddy, K. P. J, "Convective Heat Transfer Computations over Large Angle Blunt Cones Using CFX-TASCFLOW," CFX Users International Meeting, Friedrichshafen, Germany, 1999.

[24] Menezes, V., Saravanan, S., Jagadeesh, G., and Reddy, K. P. J., "Experimental Investigations of Hypersonic Flow over Highly Blunted Cones with Aerospikes," *AIAA Journal*, Vol. 41, No. 10, 2003, pp. 1955–1966.

[25] Sahoo, N., Kulkarni, V., Saravanan, S., Jagadeesh, G., and Reddy, K. P. J., "Film Cooling Effectiveness on a Large Angle Blunt Cone Flying at Hypersonic Speed," *Physics of Fluids*, Vol. 17, No. 036102, 2005, pp. 1–11. doi:10.1063/1.1862261

[26] Bardina, J. E., Huang, P. G., and Coakley, T. J., "Turbulence Modeling Validation Testing and Development," NASA TM 110446, 1997.

[27] Bardina, J. E., Huang, P. G., and Coakley, T. J., "Turbulence Modeling Validation," 28th AIAA Fluid Dynamics Conference, Snowmass Village, CO, AIAA Paper 1997-2121, 1997.

[28] Hutchinson, B. R., and Raithby, G. D., "A Multigrid Method Based on the Additive Correction Strategy," *Numerical Heat Transfer*, Vol. 9, No. 5, 1986, pp. 511–537. doi:10.1080/10407788608913491

[29] Bardina, J. E., Huang, P. G., and Coakley, T. J., "Turbulence Modeling Code Validation," AIAA Paper 1997-2121, 1997.

[30] Goldberg, U., Batten, P., Palaniswamy, S., Chakravarthy, S., and Peroomian, O., "Hypersonic Flow Predictions Using Linear and Nonlinear Turbulence Closures," *Journal of Aircraft*, Vol. 37, No. 4, 2000, pp. 671–675.

R. Cummings
Associate Editor